JOURNAL OF GEOPHYSICAL RESEARCH, VOL. 105, NO. C8, PAGES 19,631–19,647, AUGUST 15, 2000

Field observations of the wave bottom boundary layer

D. L. Foster

Department of Civil and Environmental Engineering and Geodetic Science, Ohio State University, Columbus

R. A. Beach and R. A. Holman

College of Oceanic and Atmospheric Sciences, Oregon State University, Corvallis

Abstract. This paper presents a comprehensive set of velocity and suspended sediment observations in the nearshore wave bottom boundary layer, collected during the Duck94 field experiment on the Outer Banks of the North Carolina coast. Cross-shore velocity measurements in the wave bottom boundary layer were made using five hot film anemometers, nominally spaced from 1 to 5 cm above the bed in 2 m of water depth. The time-varying location of the seabed was estimated to roughly 1 cm with a stacked set of bed-penetrating fiber-optic backscatter sensors. The instrument array was intermittently located in the surf zone on the crest of a bar. The location of the bottom varied several centimeters over a 34 min data run. Even over 4 min segments of quasi-steady statistics, occasional large waves caused short erosion and redeposition events, complicating the definition of bottom location and causing the root-mean-square velocity statistics to be nonzero below the mean bed location. This leads to obvious difficulties in comparisons with two, one-dimensional time-dependent, eddy viscosity wave bottom boundary layer models. For example, bed shears based on rms amplitude decay were lower than predicted. The observations show some evidence for a velocity overshoot region within the wave bottom boundary layer. The observations were compared with two linear eddy viscosity models. Larger estimates of a constant eddy viscosity and smaller than predicted phase leads are indicative of more rapid mixing of momentum than predicted by the models. The phase and amplitude frequency response estimated with frequency domain empirical orthogonal functions shows a nonlinear response of the wave bottom boundary layer over the incident band. These observations are among the first coherent looks at the wave bottom boundary layer under conditions of significant sediment response. They highlight the added complexity of the dynamics in natural environments.

1. Introduction

Although the wave bottom boundary layer occupies only a small part of the overall water column [O(10 cm)], it has an importance that has been recognized for many years. Because the wave bottom boundary layer is the region of fluid immediately next to the sea bed, its role in sediment suspension and bed form development and migration is crucial.

Theoretical investigations of the oscillatory boundary layer began with the idealized laminar flow solution due to a monochromatic wave on a flat, nonerodible bottom [*Stokes*, 1851] . This solution predicts an amplitude decay and a phase shift within the layer. Later investigations [*Jonsson*, 1966; *Smith*, 1977; *Grant and Madsen*, 1979] furthered this work by considering turbulent flow with vertically varying mixing and rough beds. In recent years, investigations have further incorporated rippled beds (see review by *Sleath*[1990]), more detailed turbulence modeling [*Justesen*, 1988. *Davis and Reiger*, 1977], and random waves [*Beach and Sternberg*, 1992; *Madsen et al.*, 1994; *Foster*, 1996] . These improvements have been motivated by obvious inadequacies of the early assumptions of the actual coastal ocean environment.

The controlled environment of the laboratory makes basin studies attractive for oscillatory bottom boundary layer observations, and most tests of the above theories have been based exclusively on laboratory measurements. One of the first and perhaps most referenced laboratory studies of the wave bottom boundary layer is that of /em Jonsson and Carlsen [1976]. They examined the temporal and vertical structure of a monochromatic turbulent oscillatory bottom boundary layer. Additional laboratory investigations further examined the turbulence variations over a smooth bed under monochromatic surface waves [*Hino et al.*, 1983; *Jensen et al.*, 1989]. More recently, a laboratory investigation of regular spilling breakers over a fixed hydraulically rough bed by *Cox et al.* [1996] concluded that although the oscillatory boundary layer velocity may be approximated with a logarithmic profile through most phases of the flow, it could not be predicted from linear theory. While these laboratory studies contribute to our understanding of the wave bottom

Paper number 1999JC900018.
0148-0227/00/1999JC900018$09.00

boundary layer (WBBL) under monochromatic waves, the extrapolation of these studies to a natural environment has not yet been achieved. In a comprehensive review of experimental and theoretical wave bottom boundary studies, *Sleath* [1990] , proposed that conclusions based solely on laboratory measurements will probably require substantial modification as field data becomes available.

Because of the energetic and transitory nature of the surf zone, wave bottom boundary layer observations on natural beaches are much less easily obtained than their laboratory counterparts. However, in recent years the success in making these field WBBL measurements has increased. Using a hot film anemometer in the near-bed region and visual observations, *Conley and Inman* [1992] identified a set of stages in the development of the fluid-granular boundary layer. They concluded that observed asymmetries in the fluid-granular boundary layer development were not directly related to asymmetries in the free stream wave velocity. WBBL observations on a dissipative Oregon beach showed that observed sediment suspension and turbulence variance events occurred primarily during the transition between offshore and onshore flow [*Foster et al.*, 1994] . Both of these investigations highlight the complex and presently unpredictable response of the wave bottom boundary layer to skewed and asymmetric surface waves in the natural environment.

The first field observations of the WBBL vertical structure were presented by *Trowbridge and Agrawal* [1995]. Using a vertical profiling laser Doppler velocimeter, they examined two realizations of the wave bottom boundary layer under 9 s waves with a free stream root-mean-square (rms) wave velocity of 10 cm/s in a 6 m water depth. Examining cross-shore flows, they observed an increase in phase lead and a slight decrease of variance with increasing proximity to the bed and concluded that the observed scales were characteristic of simple theoretical wave bottom boundary models.

The observations presented here are the first surf zone measurements to examine the temporal and vertical variations of wave bottom boundary layer dynamics with simultaneous measurements of the bed elevation and vertical distribution of suspended sediment under wave conditions for which bed response is important. The unique nature of these observations allows us to evaluate predictions from both a monochromatic and a random wave bottom boundary layer models.

In this paper we evaluate two existing simple WBBL models with field observations made during the Duck94 field experiment. In section 2, the two theoretical models for the wave bottom boundary layers are reviewed. In section 3, the instrumentation and the field measurement techniques are summarized. An interpretation of field results and model comparisons are presented in the discussion, section 4, and conclusions are presented in section 5.

2. Models

2.1. WBBL Theory

The one-dimensional, time-dependent wave bottom boundary layer governing equation is

$$\frac{\partial u}{\partial t} - \frac{du_\infty}{dt} = \frac{1}{\rho}\frac{\partial \tau}{\partial z}, \tag{1}$$

with boundary conditions,

$$u(\delta, t) = u_\infty,$$

$$u(z_o, t) = 0,$$

where $u = u(z,t)$ is the cross-shore velocity, $u_\infty = u_\infty(t)$ is the free stream velocity, z_o is the bed roughness, and δ is the boundary layer thickness. Throughout this paper, the vertical elevation ,z, is positive upward from the bed, and the cross-shore position ,x, is positive offshore. In both models evaluated here, the shear stress ,τ, is estimated with an eddy viscosity model

$$\frac{\tau}{\rho} = -\langle u'w' \rangle \approx \nu_t \frac{\partial u}{\partial z}, \tag{2}$$

where ρ is the fluid density, ν_t is the eddy viscosity, u' is the cross-shore turbulent velocity, and w' is the vertical turbulent velocity. Assuming that all turbulence is initiated at the bed and proportional to elevation, the eddy viscosity is approximated with [*Smith*, 1977; *Grant and Madsen*, 1979]

$$\nu_t \equiv \kappa u_* z, \tag{3}$$

where u_* is the bed shear velocity and $\kappa (= 0.41)$ is von Karman's constant.

2.2. WBBL Velocity Under a Single Monochromatic Wave

The first model evaluated in this paper, based on that of *Smith* [1977], represents the true free stream velocity with a single representative monochromatic wave with free stream amplitude ,u_o, and frequency ,ω. The boundary layer thickness and shear velocity are parameterized with constant values defined with the equations:

$$\delta_{sm} = \frac{u_{*sm}}{2\omega}, \tag{4}$$

$$u_{*sm} = \frac{\kappa u_o}{ln\left(\frac{\delta_{sm}}{z_o}\right)}, \tag{5}$$

where δ_{sm} is the representative boundary layer thickness of the monochromatic wave, as defined *Beach and Sternberg* [1992], and u_{*sm} is the representative shear velocity. The cross-shore wave bottom boundary layer velocity ,u_s, at the specified characteristic frequency that satisfies (1) is

$$u_s(z,t) = u_o \Re \left\{ e^{i\omega t} [1 - Z(z)] \right\}, \tag{6}$$

where $Z(z)$ is the complex spatial amplitude. The spatial amplitude is determined by substituting (6) into (1) and solving the resulting equation analytically, yielding a solution of

$$Z(z) = \frac{K_o(y_o)I_o(y) - I_o(y_o)K_o(y)}{K_o(y_o)I_o(y_\delta) - I_o(y_o)K_o(y_\delta)}, \tag{7}$$

where

$$y(z) = 2\left\{\frac{\omega z}{\kappa u_{*sm}}\right\}^{1/2}, \quad (8)$$

note $y_o = y(z_o)$ and $y_\delta = y(\delta)$. Although this model cannot predict the velocity structure at each instant in time under a random wave field, it is possible to predict the vertical amplitude and phase structure, as well as the boundary layer thickness, and shear velocity at the characteristic frequency. Here we choose the characteristic frequency ,ω, to be the peak frequency and the amplitude (u_o) to be $u_o = \sqrt{2}u_{\infty_{\text{rms}}}$, where $u_{\infty_{\text{rms}}}$ is the free stream rms velocity over an entire record.

2.3. WBBL Velocity Under a Random Wave Field

The second model is based on the same dynamics as the *Smith* [1977] model but allows for an arbitrary random wave forcing and a time-varying eddy viscosity; see *Foster et al.* [1999] (hereafter referred to as FGH) for the complete solution method and model evaluation. The FGH model satisfies (1) with an analytical eigenfunction series solution by assuming the eddy viscosity is a separable function of time and space. As in FGH, we assume

$$\nu_t = \kappa u_{*\text{FGH}}(t) z, \quad (9)$$

where $u_{*\text{FGH}}(t)$ is the bed shear velocity. The complete series solution is

$$u_{\text{FGH}}(z,t) = \sum_{n=1}^{\infty} a_n(t)\Psi_n(z) + \frac{z - z_o}{d - z_o}u_\infty, \quad (10)$$

where a_n is the amplitude of the nth spatial eigenfunction [$\Psi_n(z)$] and d is the top of the domain and is greater than the boundary layer thickness. Here, we assume the top of the domain is the location of the current meter located in the free stream. The eigenfunction $\Psi_n(z)$ is defined as

$$\Psi_n(z) = Y_o(2\lambda_n z_o^{1/2})J_o(2\lambda_n z^{1/2}) - J_o(2\lambda_n z_o^{1/2})Y_o(2\lambda_n z^{1/2}), \quad (11)$$

where λ_n are the eigenvalues and J_o and Y_o are zero-order Bessel functions of the first and second kind, respectively. The eigenvalues are determined by solving

$$Y_o(2\lambda_n z_o^{1/2})J_o(2\lambda_n d^{1/2}) - J_o(2\lambda_n z_o^{1/2})Y_o(2\lambda_n d^{1/2}) = 0. \quad (12)$$

The amplitude is determined by

$$a_n(t) = a_n(0)e^{-\lambda_n^2 \int_o^t \kappa u_{*FGH}(\tau)d\tau} + \int_0^t F_n(\sigma)e^{-\lambda_n^2 \int_\sigma^t \kappa u_{*\text{FGH}}(\tau)d\tau}d\sigma, \quad (13)$$

where the forcing is

$$F_n(t) = \frac{1}{c_n}\int_{z_o}^{d}\left(\frac{d-z}{d-z_o}\frac{du_\infty}{dt} + k u_{*\text{FGH}}(t)\frac{u_\infty}{d-z_o}\right)\Psi_n(z)dz. \quad (14)$$

c_n is the orthogonality constant and defined by

$$c_n = \int_{z_o}^{d}\Psi_n(z)\Psi_n(z)dz. \quad (15)$$

As the bed shear velocity is initially unknown, it is estimated with (5) as a constant value over every free stream zero crossing. After the first iteration, the bed shear velocity is directly calculated with

$$u_{*\text{FGH}}(t) = \kappa z_o \left|\frac{\partial u(z,t)}{\partial z}\right|_{z=z_o} \quad (16)$$

and iterated until the solution converges. Both models assume a constant bed elevation and known bed roughness. Using both models, we will estimate the time- and depth-dependent cross-shore velocity, the boundary layer thickness, and the bed shear velocity.

3. Observations

3.1. Deployment

Field observations were made at the Army Corps of Engineers, Field Research Facility (FRF) in Duck, North Carolina from August 14, 1994 to August 23, 1994 as part of the cooperative Duck94 experiment. During the experiment the significant wave height varied from 0.5 to 1.5 m and the significant wave period varied from 4 to 14 s. A variety of bed conditions were observed.

The following investigation focuses on one 34 min run recorded on August 17, 1994. The significant offshore wave height, angle, and period measured at the 8 m depth were 0.83 m, 50° from the southeast, and 4.54 s, respectively. The mean onshore and alongshore current were 2 cm/s offshore and 6 cm/s to the north, respectively. The observations presented in this paper were made in 2 m water depth on the bar crest under both broken and unbroken waves. Visual observations, made using divers and a continuously recording underwater video camera, indicate a well sorted, flat bed with infrequent ripples. Multiple sediment samples showed a median grain diameter of 0.18 mm (D. Stauble, personal communication, 1996).

Instruments were deployed from a cantilevered arm attached to the lower boom of the sensor insertion system (SIS) on the pier at the FRF (Figure 1). The angles of both the upper and lower booms were adjusted to keep sensors at least 20 m from the pier. The angle of the cantilever arm relative to the lower boom was set to assure the cantilever arm was parallel to the bed. A spike attached to the lower boom of the SIS was set into the bed with the weight of both booms, fixing the position of the array. An accelerometer, located near the base of the lower boom, indicated the rms displacement and velocity over the entire record was less than 1 mm and 1 cm/s in any direction over the 30 min record. The SIS displacement was largest during the latter 10 min of the 30 min record under large, vertically accelerating wave crests.

3.2. Instrumentation

WBBL velocity observations were made with a vertical array of five hot film (HF1-HF5) anemometers, in the lower 5 cm of the water column with a 1 cm array spacing. A Marsh-McBirney electromagnetic current meter (EMCM) measured the cross-shore and alongshore velocity outside the boundary layer at approximately 14 cm above the bed. Sediment suspension and bed elevation were measured with a 19 sensor fiber-optic backscatter (FOBS) probe. Sea surface elevation observations were made using two strain gage pressure sensors. The presence of bed forms was determined using observations from an underwater video camera. The relative location of all instruments is shown in Figure 1.

Hot film anemometers estimate the local fluid speed by assuming that the heat transfer between a constant temperature wire (and a protective film coating) and the ambient fluid is a function of the fluid speed. In this experiment, the 0.0152 mm diameter film was heated to approximately 25°C above ambient water temperature. The voltage output is a measure of the convective cooling of the film due to the surrounding fluid and is related to the magnitude of fluid velocity flowing past the film. The output signal for the probe with the longitudinal axis aligned in the alongshore direction is defined by [*George et al.*, 1994; *Foster*, 1996]

$$S(t) \propto (u_T^2 + \beta v_T^2 + w_T^2)^{1/2}, \tag{17}$$

where β is a parameter that accounts for the relative longitudinal (y) to normal (x and z) heat transfer and is assumed to be small ($\beta \ll 1$). The total cross-shore, alongshore, and vertical velocities, u_T, v_T, and w_T, respectively, are partitioned into mean(overbar), wave(tilde), and turbulent(prime) components. Here it is assumed that the cross-shore velocity is the dominant wave velocity ($\tilde{u} \gg \tilde{v}\tilde{w}$), and the mean velocities are small with respect to the wave velocity ($\tilde{u} \gg \bar{u}, \bar{v}, \bar{w}$). Furthermore, it is assumed that the wave velocity is larger than the turbulent velocity ($\tilde{u} \gg u'$) and that turbulence is isotropic ($u' \sim v' \sim w'$), leading to

$$S(t) = \left[\tilde{u}^2 + 2\tilde{u}u'z + O(u'^2)\right]^{1/2} \approx |\tilde{u} + u' + O(u'^2)|. \tag{18}$$

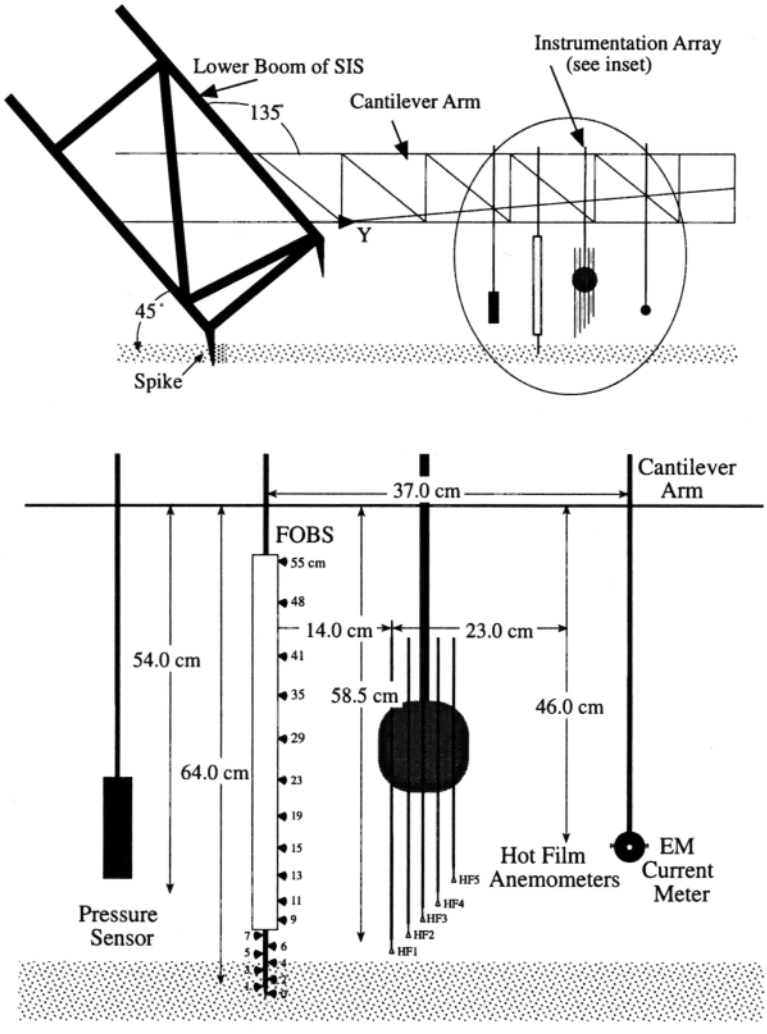

Figure 1. Diagram of cantilever and instrumentation. Inset at bottom shows close-up view of hot film anemometers, fiber-optic backscatter sensor (FOBS) probe, and electromagnetic current meter. Note that actual elevation from the bed varies over the data run.

To first order, it is assumed that the hot film output is a measure of the cross-shore wave and turbulent velocity magnitude. See *Foster* [1996] for an analysis of the probe's frequency response.

Sediment suspension and bed level elevation were measured with a fiber-optic backscatter sensor (FOBS) probe [*Beach et al.*, 1992] . Light pulses emitted through the each of the FOBS's 19 optical fibers at 850 Hz are filtered to and sampled at 16 Hz. The instrument is composed of two distinct probes (Figure 1). The smaller tapered lower probe contains eight 600 μm fiber-optic sensors, each contained within a 2 mm stainless steel tube and vertically separated from the other sensors by 1 cm. To avoid interference between neighboring sensors, the sensor array elements are staggered around the probe. The larger, upper probe contains 11 sensors with vertical spacing varying from 2 to 6 cm. The combination of both probes covers a total vertical range of 55 cm. The FOBS probe is calibrated in a fully turbulent, well-mixed tank with the same procedure as outlined by *Beach et al.* [1992]. A transfer function between concentration and FOBS output voltage is defined with a quadratic curve.

In addition to measuring sediment suspended in the water column, the FOBS also provides for measurement of the bed elevation. By piercing the bed, bed level fluctuations of 1 cm or more are monitored as sensors are alternatively buried and exposed by bed accretion and erosion, respectively. The lower probe tapers to 2 mm at the lowest sensor, enabling the probe to pierce the bed with minimal interference and scour. When a sensor measures a sustained large concentration, it is assumed to be buried. Often, when the sensor is at the bed-water interface a concentration between the maximum saturated value and the normal background concentration is sustained.

3.3. Hot Film Calibration and Data Quality

Prior to each data run, the hot film probes were positioned at the same elevation as the EMCM, the boom of the SIS was lowered into position, and a 10 min calibration data set was collected. During the calibration period, the elevation of the bed was determined with the FOBS. Following the calibration period, the instruments were raised out of the water, the hot films were positioned at the desired elevation based on FOBS estimate of the bed location during the calibration run, the boom was relowered back into the water column, and data were recorded for 34 min.

Time synchronization between the five hot film anemometers, one pressure sensor, and the electromagnetic current meter was achieved by sampling the instruments with the same data acquisition system at 2000 Hz. The pressure sensor and current meter were fed through an optical isolator to prevent interference, as they were also sampled on another data acquisition system for a companion experiment not discussed here. The effect of the optical isolator on the gain was removed during calibration. Also removed during calibration was the effect of the internal electromagnetic current meter 5 Hz fiive pole Bessel filter. An additional pressure sensor and the FOBS were sampled at 16 Hz with a third independent data acquisition system. Both the hot film and FOBS data acquisition systems were time synchronized with a Global Positioning System (GPS) time code receiver.

The hot film sampling system included a 30.55 Hz analog one pole filter. The effect of the filter was removed by computing the fast Fourier transform (FFT) of 66,000 points of data (33 s) for each channel and then dividing out the known response of the filter. To prevent the amplification of noise, the filter response was only removed up to 150 Hz, the limit of high signal-to-noise ratio. Consequently, each record was digitally low-pass filtered in the frequency domain with a cutoff frequency of 128 Hz and resampled at twice the cutoff frequency, 256 Hz, to 8448 points before converting back to the time domain with an inverse FFT. Each 33 s segment is overlapped with the previous and following data segments by 1 s to eliminate the effect of side lobes caused by the boxcar window. The resulting effective Nyquist frequency is 128 Hz.

The hot film anemometers were calibrated over incident wave frequencies with the EMCM. Each hot film channel was block averaged to 16 Hz to remove some high frequency (turbulent) variability and maintain the variance required to resolve the sharp accelerations caused by the inherent rectification of the hot film signal, and the EMCM was digitally filtered to 2 Hz. The cross correlation between each hot film and the magnitude of the EMCM was computed over consecutive 10 s increments. Each 10 s of data for which the squared cross-correlation coefficient was greater than $0.7(\gamma^2 > 0.7)$ was used in the calibration. For the five hot film sensors in this run, from 23% to 68% of the data were accepted. Data that passed this criteria were fit to a logarithmic curve using a nonlinear least squares fit ($|u| = \alpha e^{\beta(\text{volts})}$). Table 1 gives the coefficients, α and β, for each log fit. Although the expected response for a hot film anemometer is quadratic, a logarithmic curve does not have the potential to yield a minimum within the domain (a possibility that may occur with a quadratic fit) and resulted in statistically acceptable fits. The F statistic, significance level, and root-mean-square deviation (rmsd) between each hot film sensor and the calibration curve are given in Table 1. The root-mean-square deviation and F statistic reported in Table 1 include the high-frequency fluctuations of each HF beyond the incident band, out to 16 Hz. The uppermost hot

Table 1. Hot Film Calibration Coefficients, α and β

Hot Film Sensor	α, cm/s	β, 1/volts	rmsd, cm/s	F,	Sig. Level, %
1	0.24	0.76	8.92	5.4	99.5
2	0.51	0.62	8.58	5.3	99.5
3	0.12	0.84	8.77	5.6	99.5
4	0.55	0.62	10.87	3.6	97.25
5	1.48	0.48	15.54	10.0	61.25

The F statistic between the logarithmic transfer function and each hot film sensor yields significance levels of at least 97% in sensors 1-4. Here rmsd is root-mean-square-deviation.

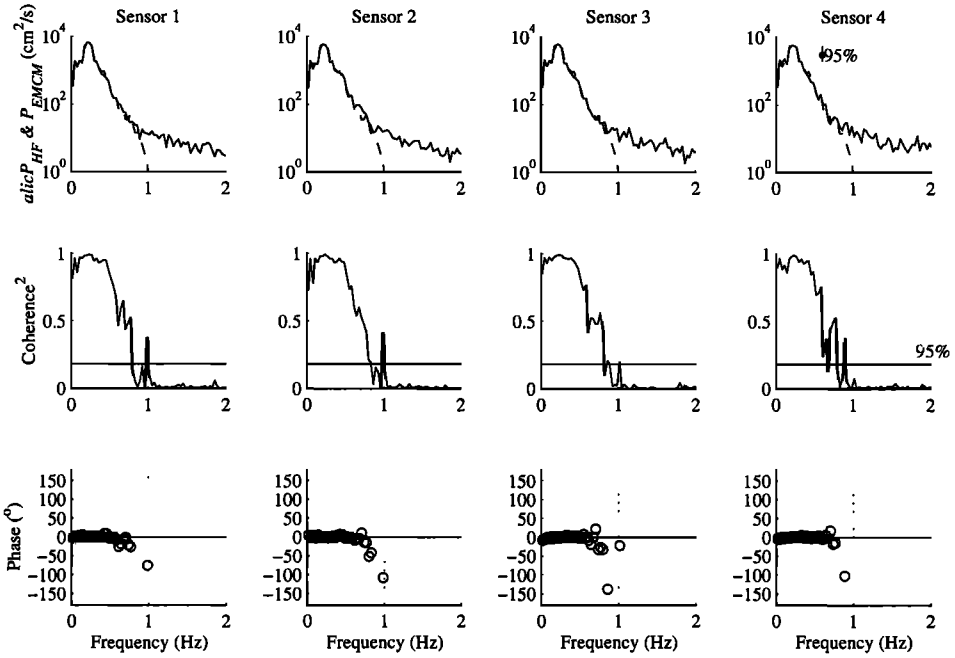

Figure 2. Coherence and phase between the calibrated derectified cross-shore velocity as measured by hot film sensors 1-4 (solid curve) and cross-shore velocities as measured by the electromagnetic current meter (dotted curve). The coherence remains significant to 0.8 Hz. Each spectrum has been calculated with 32 degrees of freedom.

film sensor, HF5, had an unstable gain, possibly owing to oxidation of organics, resulting in a low significance level of 61.25% and consequently, was excluded from further investigation. Owing to the close proximity to the seabed (and distance from surface breaking), dropouts due to bubbles were absent. The sign of the calibrated hot film signal is determined by searching for local minima around each zero crossing of the cross-shore EMCM velocity. Throughout this paper, the onshore directed flow is negative and offshore directed flow is positive. The cross spectrum between each calibrated, derectified hot film velocity and the cross-shore EMCM velocity shows that the two measurements are coherent out to approximately 0.8 Hz (Figure 2). The integrated variance of the incoherent signal between each HF and the EMCM over the incident wave frequency to 1 Hz, is represented by

$$\varepsilon^2 = \int_{f=0}^{f=1} (1-\gamma^2)(P_{\mathrm{HF}} P_{\mathrm{EMCM}})^{1/2} df \qquad (19)$$

where ε is the integrated deviation between each HF and the EMCM over the frequency ,f, band of interest, γ is the coherence, and P is the energy density spectrum. Good agreement exists between the calibrated, derectified cross-shore velocities as predicted by the four hot film sensors and EMCM with deviations ε ranging from 6–8 cm/s (Figure 3).

Because the hot films were in the region of active sediment suspension, the effect of sediment on the probe response was determined by examining the variation of the thermal diffusivity, kinematic viscosity, density, and specific heat of the fluid surrounding the probe with and without sediment. Under a maximum sediment concentration of 160 g/L, the theoretical probe response increased by 5% and this effect was consequently neglected. The complete theory and analysis are given by /em Foster [1996].

The bed elevation was determined by identifying the highest buried sensor at 1 s intervals (Figure 4, bottom). At each s, a sensor was assumed buried when the median concentration over a centered 30 s window was at least 10 g/L. An exception to this rule was made for sensor 6, which was faulty, perhaps owing to a cracked fiber, resulting in anomalously high concentrations. Although this sensor cannot be used for quantitative suspended sediment investigations, it is sensitive to burial. In this investigation, sensor 6 detected the seabed at an anomalous concentration of 400 g/L. The resolution of this estimate at the FOBS probe was assumed to be plus/minus one half of the separation between the neighboring FOBS sensors. The maximum slope difference between the bed and instrument cantilever was estimated as 2° resulting in an additional potential uniform bed elevation uncertainty between the FOBS and the hot film array of 0.5 cm.

4. Results

4.1. Evidence of the WBBL

To acquaint the reader with the observations, Figure 5 shows a 2 min time series segment of the four near-bed velocities, measured by the calibrated, derectified hot films (HF1-4), and the free stream velocity, measured by the EMCM. The near-bed velocity records show fluctuations over both wave and turbulent bands. Consistent with WBBL theoretical predictions, the near-bed HF observations show strong

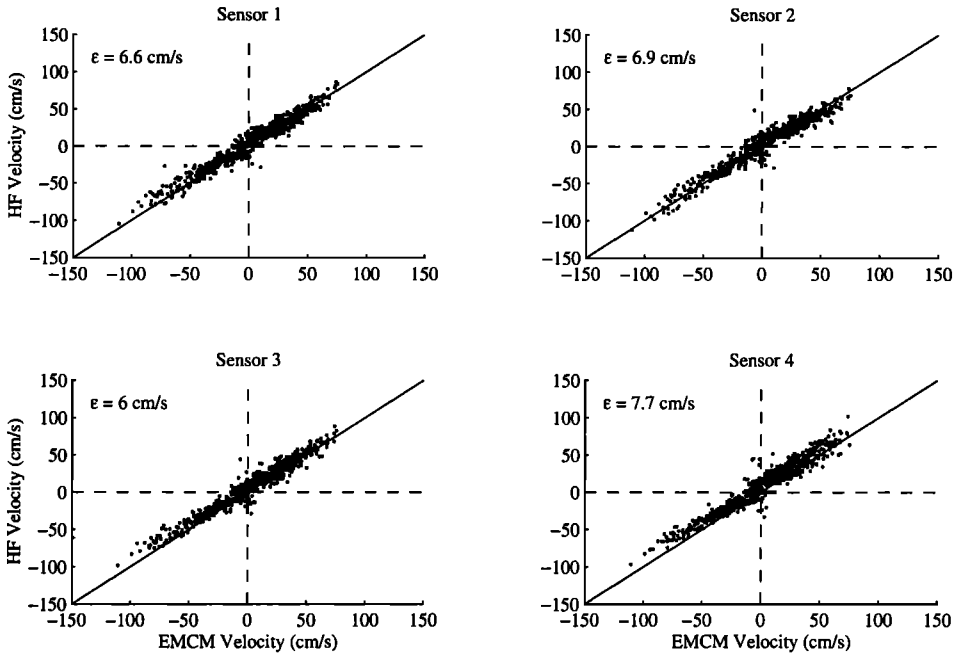

Figure 3. Comparison of the cross-shore velocities as measured by the electromagnetic current meter (EMCM) and the calibrated, derectified cross-shore velocities as measured by hot film sensors (HF1-HF4). Each record has been digitally low-pass filtered to 1 Hz. The rms deviation, ε, between the EMCM and each HF is specified for each comparison.

coherence but exhibit a decrease in wave amplitude with decreasing sensor elevation. Near-Bed flow amplitudes are still large; at 0.9 cm above the bed there exists a strong wave signal with maximum velocity magnitudes of up to 100 cm/s. Also visible in the hot film records are the turbulent fluctuations, which are of significantly lower magnitude and generally increase with increasing free stream velocity.

A sample 20 s time series, which has been filtered with a 1 Hz low-pass filter to isolate the wave frequencies, also shows a decrease in amplitude with proximity to the bed (Figure 6).

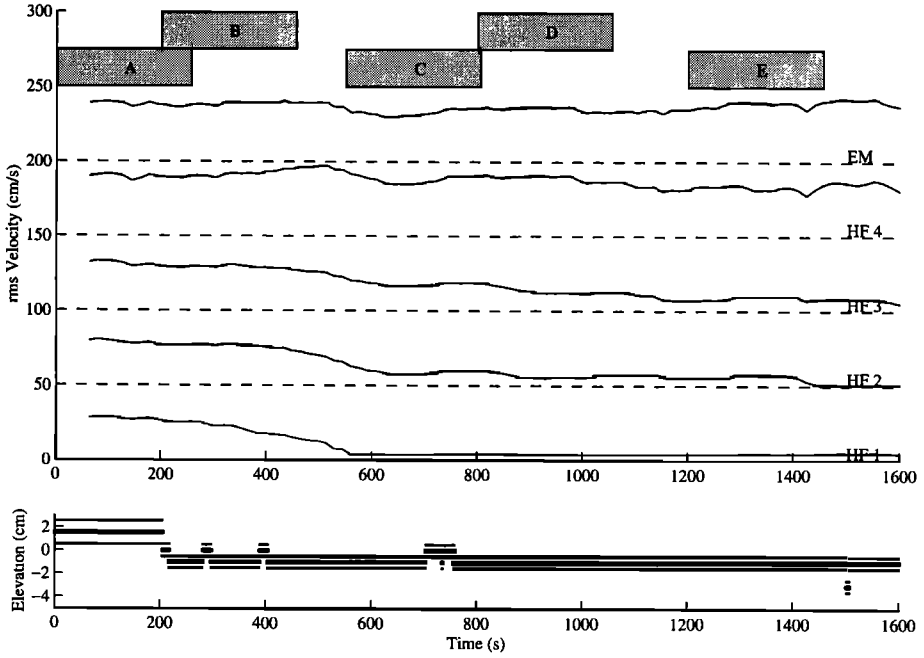

Figure 4. (top) Time-varying root-mean-square velocity at five elevations above the bed over consecutive 128 s windows. Each record is offset from the previous by 50 cm/s. The array spacing of HF1 - HF4 is 1 cm. The shaded bars labeled A-E indicated five 256 observation segments. (bottom) Distance of lowest hot film (HF1) to bed as estimated by the FOBS. Note that negative elevations indicate that HF1 is buried. The maximum possible error bounds each estimate and is indicated with the thinner lines.

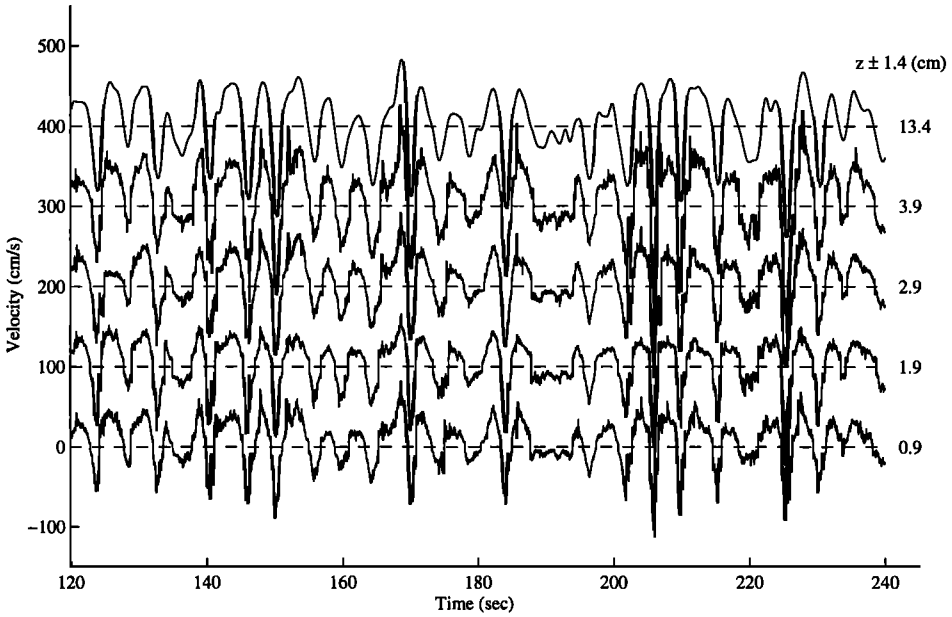

Figure 5. A 2 min time series of the derectified calibrated velocity as measured by fur hot film anemometers within the wave bottom boundary layer and in the free stream as measured by an EMCM. The average distance of each sensor from the bed as measured by the FOBS over the 2 min record is listed at right. Each time series is offset from the others by 100 cm/s. Onshore directed flow is indicated with negative velocities, and offshore flow is indicated with positive velocities.

Peak negative velocities (wave crests) at the lowest elevations occur prior to the peak at subsequent upper sensors. This is consistent with simple theory, which predicts a phase lead relative to free stream velocity (or potential flow) with increasing proximity to the bed.

An example of the vertical structure of the cross-shore velocity over two consecutive waves in Figure 6 (224 to 234 s) is shown in Figure 7. In agreement with the phase lead predicted by simple theory, the sensors closest to the bed in Figure 7, panels labeled II and III, reverse direction prior to

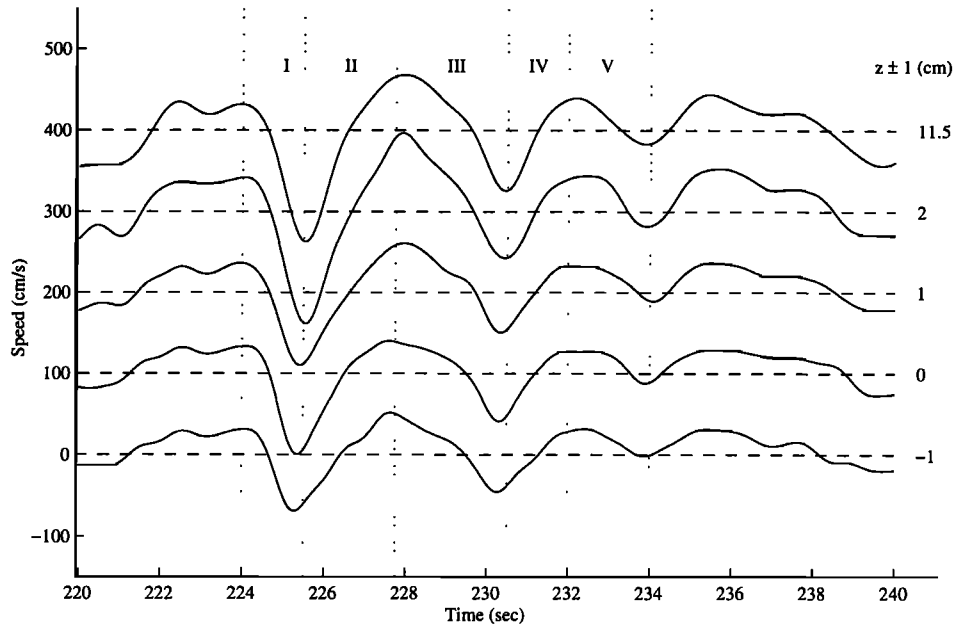

Figure 6. An example 20 s time series of the near-bed velocities showing the amplitude decay and phase lead in the lower sensors, which is consistent with the simple wave bottom boundary layer theory. Each sensor has been digitally low-pass filtered to removed turbulent fluctuations higher than 1 Hz. Each time series is offset from the previous by 100 cm/s.

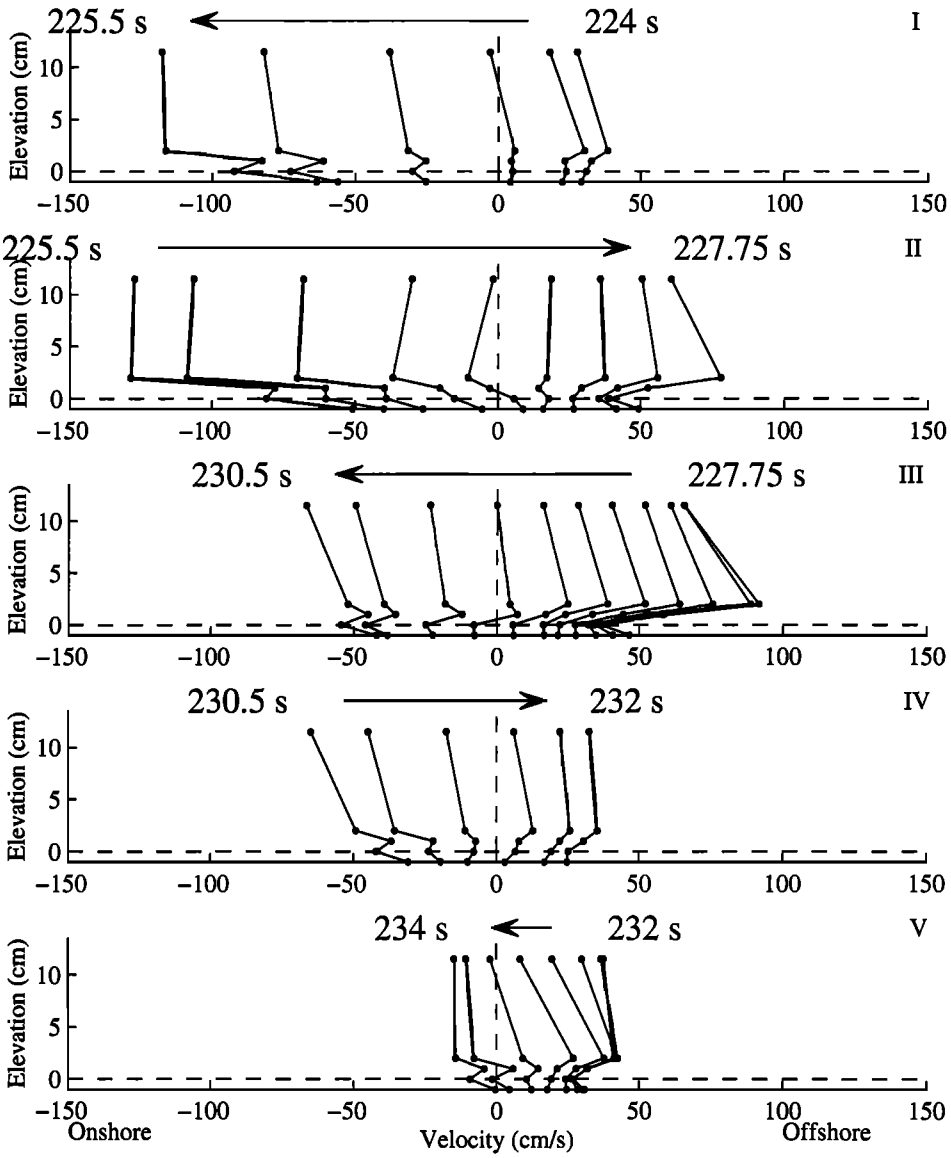

Figure 7. Vertical structure of low-passed cross-shore velocity at the five 0.25 s intervals (labeled I, II, III, IV, and V) as specified in Figure 6. Arrows indicate the direction of time between samples. Dashed line indicates assumed bed elevation.

the free stream velocity reversal. However, this phenomenon is not present in the preceding and following smaller waves, see Figure 7, I and V. Larger vertical shears of the cross-shore velocity are present in the first 5 s (224.5 to 229.5 s) wave than in the following, smaller-amplitude 3.5 s (229.5 to 233 s) wave. Although the general trend of the velocity is to decrease with decreasing elevation, there still exists significant complexity in the vertical structure. Large velocities are present in the sensors that are closest to the bed; for example in Figure 7, II, the velocity is as large as 50 cm/s at -1 cm above the bed. The scaling of these two waves suggests visual support for the premise that the boundary layer thickness and bed shear velocity scale with wave frequency and free stream wave amplitude, as in (4) and (5). This is more rigorously tested at the end of this section. Also, the change in the boundary layer structure over the two consecutive waves implies that the boundary layer may respond to changing free stream wave forcing within a wave period.

4.2. Statistical Boundary Layer Scalings

The seabed elevation trended upward over the course of the 34 min record; consequently the record was partitioned into five (A-E) quasi-stationary, 256 s segments of data during which the bed elevation could be assumed constant and SIS vibration remained relatively small. The variance appeared relatively uniform at each elevation and over each segment (Figure 4). For each 256 s data segment, the bed elevation was represented by the average bed elevation. The input wave conditions over the five segments were unchanged.

The velocity spectra for segments A and C show that for three of the four hot film sensors the total velocity variance

decreases with proximity to the bed (Figure 8). The velocity variance for all sensors within the WBBL in segment C is lower than that in segment A because the bed accreted between the two runs and caused the sensor array to be closer to the bed. A break in slope of the HF spectra occurs around 1 Hz and may be indicative of a shift from dominance of wave motions to dominance of turbulent motions. This break is less obvious in sensors that are closer to the bed which have lower incident band energy. This may be attributed to WBBL nonlinearities whose energy transfer from the incident to higher frequencies is highest near the bed [*Trowbridge and Madsen*, 1984; FGH]. Also, motions closest to the bed may have a different frequency at which turbulence begins, owing to the smaller length scales ($f \sim u/z$). The linear wave theory deep water wave for a 2 m water depth would suggest a lower frequency cutoff of approximately 0.6 Hz. Because of the nonlinearities present in the WBBL and the spectral slope break, we have chosen a cutoff based on the observations of 1 Hz.

The rms velocity for each segment (A-E) at each elevation is shown in Figure 9. An allowance was made for variation in the estimate of the bed elevation by adding and subtracting the time-averaged maximum error as estimated in the previous section (Figure 4) to the average bed elevation over each record (see vertical error bars in Figure4). The rms deviation over the incident band between the EMCM and each HF, ε, as determined during calibration (see Figure 3) is indicated with horizontal bars. With the exception of HF4 in segments A-D, the variance decreases with decreasing sensor elevation, showing similar trends in all five segments. When a sensor is assumed to be buried (negative elevations), as in segments D and E, the rms velocity is nonzero and can largely be attributed to large onshore velocities that temporarily vertically displace the SIS or mobilize the bed (e.g., Figure 10). Occasional crests can mobilize the bed, expose buried sensors, and suspend sediment in the water column. Following passage of the wave, the sediment settles out of the water column and reburies the sensors. This example

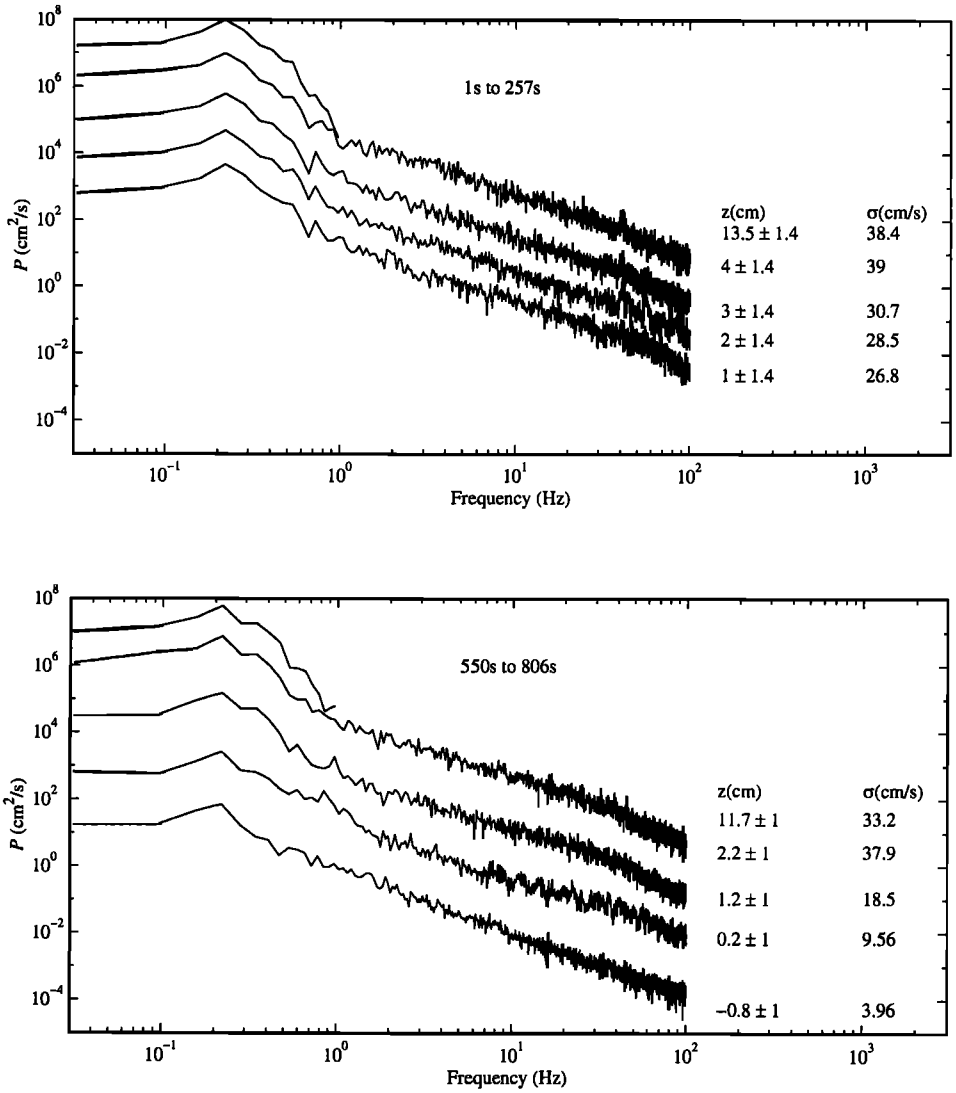

Figure 8. Energy density spectra as a function of frequency over segments (top) A and (bottom) C. Each sensor is offset by 1 decade from the previous sensor. Right-hand columns show the time-averaged bed elevation estimate of the record and the standard deviation at each elevation.

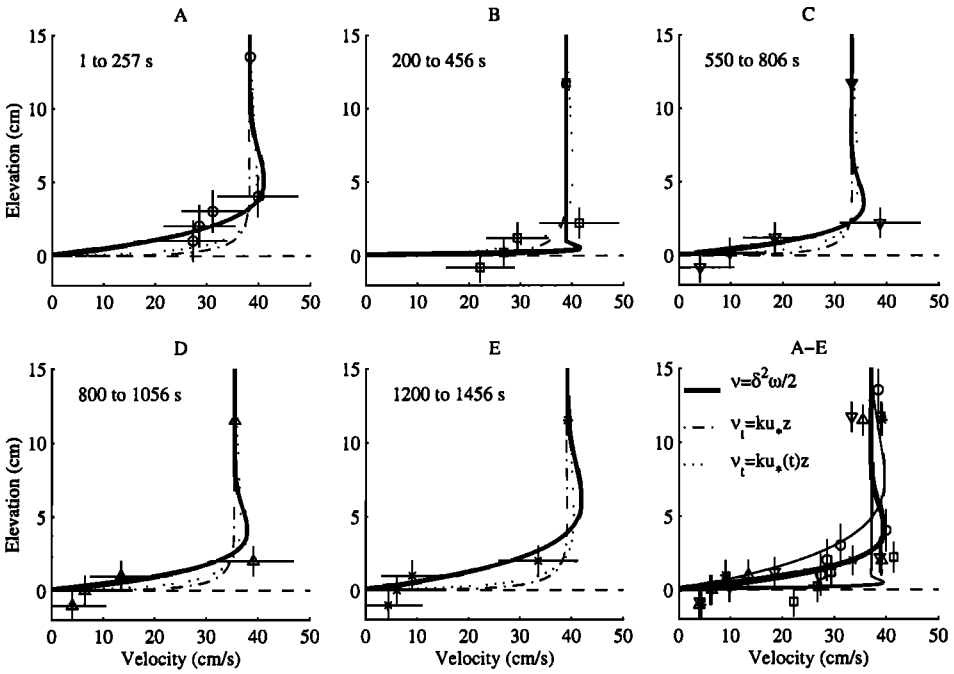

Figure 9. The root-mean-square (rms) velocity over each segment (labeled A-E) of the observations (various symbols), constant eddy viscosity model (solid curve), *Smith* [1977] linear eddy viscosity model (dot-dashed curve) and the FGH time-varying linear eddy viscosity model (...). The vertical error bars indicate the maximum deviation in bed estimate of each quantity about the observations. The horizontal bars about the data indicate $\pm\varepsilon$ (19). Panel labeled A-E shows all of the observations and the constant viscosity model (bold line). Also, it shows the constant viscosity model results if the bed variation is moved plus/minus the maximum bed estimation error (nonbold lines).

highlights the difficulty of applying simple theory to the observations when the bed location is variable and represented with a statistical quantity.

The bed roughness, z_o, was estimated with an empirical formulation for a turbulent, hydraulically rough, movable bed. Following *Nielsen* [1992], the physical roughness, $z_o = r/30$, depends uniquely on the hydraulic roughness, r,

$$r = 170(\theta_{2.5} - 0.05)^{0.5} d_{50}. \tag{20}$$

The grain roughness shields parameter, $\theta_{2.5}$, is defined by

$$\theta_{2.5} = \frac{\frac{1}{2} f_{2.5} \rho (A\omega)^2}{\rho(s-1) g d_{50}}, \tag{21}$$

where A is the free stream orbital amplitude, s is the specific density of the sediment (2.65), d_{50} is the median grain diameter (.18 mm), and $f_{2.5}$ is the grain roughness friction factor. The grain roughness friction factor is defined by

$$f_{2.5} = e^{[5.213(\frac{2.5 d_{50}}{A})^{0.194} - 5.977]}. \tag{22}$$

For this investigation the orbital amplitude was defined by $A = \sqrt{2} u_{\infty_{\text{rms}}}/\omega$, where ω is the mean peak frequency for each of the five independent runs and $u_{\infty_{\text{rms}}}$ is the mean rms free stream velocity, as measured by the EMCM, of the five independent runs. The resulting mean bed roughness assumed for the following investigations is 0.68 mm.

The rms velocity observations are compared with a constant eddy viscosity model, in a manner analogous to laminar flow theory for a Stokes boundary layer. Assuming hydraulically rough flow and a monochromatic free stream wave, the velocity solution is

$$u(z,t) = u_o\left[1 - e^{-\frac{z-z_o}{\delta_c}(i+1)}\right] e^{i\omega t}, \tag{23}$$

where $\delta_c = \sqrt{2\nu_c/\omega}$ is a measure of the mixing length scale and ν_c is the constant eddy viscosity governing the mixing. Note that for laminar flow, $\nu_c = \nu$ and $\delta_c = \delta_s$, where δ_s is the Stokes boundary layer thickness. The single free parameter, δ_c, is determined with a nonlinear least squares fit to all of the rms velocity observations that had sensor elevations greater than the bed roughness, $z > z_o$. Comparisons with the observations are shown in Figure 9. Comparisons with the observations, assuming $\pm\Delta z$ the maximum bed position error, show the sensitivity of the results to the assumed bed position (see Figure 9, bottom right).

For each data segment, the monochromatic Smith [1977] model was evaluated at the peak frequency with a free stream amplitude chosen to match the total free stream velocity variance. The Smith model predicts an rms velocity structure of the same order of magnitude as the observations but generally predicts larger near-bed velocity shear and a smaller boundary layer thickness than is present in the observations (Figure 9). The rms deviation between the measured and calculated rms velocity profiles is defined with

$$[\Delta u_{S_{\rm rms}}(z)]_{\rm rms} = \left\{\frac{1}{N}\sum_{n=1}^{N}[u_{S_{\rm rms}}(z_n) - u_{D_{\rm rms}}(z_n)]^2\right\}^{1/2}, \quad (24)$$

where N is the number of hot films ($N = 4$) and u_D is the measured velocity at each elevation. Note that the model velocity is assumed to be zero at elevations less than the bed roughness height. Here $[\Delta u_{S_{\rm rms}}(z)]_{\rm rms}$ has a mean value over the five segments, $\langle[\Delta u_{S_{\rm rms}}(z)]_{\rm rms}\rangle$, of 9.7 cm/s and is given for each of the five segments in Table 2. Note that

$$\langle a\rangle = \frac{1}{5}\sum_{p=1}^{5} a_p$$

indicates the average of any given quantity, a, over the five data segments, and

$$\bar{a} = \frac{1}{N}\sum_{n=1}^{N} a_n$$

indicates the vertical average over the four hot film sensors.

The rms velocity structure predicted by the FGH model for each data segment is also compared with the observations and the Smith model in Figure 9. The model is forced with the free stream velocity at 14 cm above the bed and constant bed roughness given above. The rms velocity structure predicted by the FGH model has similar shape to the Smith model with high near-bed velocity gradients and a small boundary layer thickness compared to the constant viscosity model (Figure 9). As defined in (21), the rms deviation between the measured and FGH model predicted rms velocity has a mean value, $\langle\overline{[\Delta u_{\rm FGH_{rms}}(z)]_{\rm rms}}\rangle$, of 10.6 cm/s and is given for each of the five segments in Table 2. The rms deviation spatially averaged over the HF sensor array between the time varying FGH model calculations and the observations is defined by

$$\overline{[\Delta u(z,t)]_{\rm rms}} = \frac{1}{N}\sum_{n=1}^{N}\left\{\frac{1}{M}\sum_{m=1}^{M}(u_{\rm FGH}[z_n,t_m) - u_D(z_n,t_m)]^2\right\}^{1/2} \quad (25)$$

where M indicates a summation over time (for each independent segment) and N indicates a summation over space. Table 3 shows statistics for the mean value, $\langle\overline{[\Delta u(z,t)]_{\rm rms}}\rangle$, 13.2 cm/s, and for each data segment.

The WBBL mixing is evaluated with the bed shear velocity, u_*, and with the shear length scale, u_*/ω. First, a logarithmic model that assumes the turbulent mixing depends on the velocity shear at the bed is evaluated. For this case, the shear velocity of the rms velocity observations was estimated with the formulation in (16) by

$$u_{*\log} = \kappa z_o \left|\frac{\partial u}{\partial z}\right|_{z=z_o} \quad (26)$$

The velocity gradient at the bed is approximated with the rms observations,

$$\left|\frac{\partial u}{\partial z}\right|_{z=z_o} \approx \sqrt{2}\left[\alpha u_{\rm rms}(z_o) + \beta u_{\rm rms}(z_o+\Delta z_1) + \gamma u_{\rm rms}(z_o+\Delta z_2)\right] \quad (27)$$

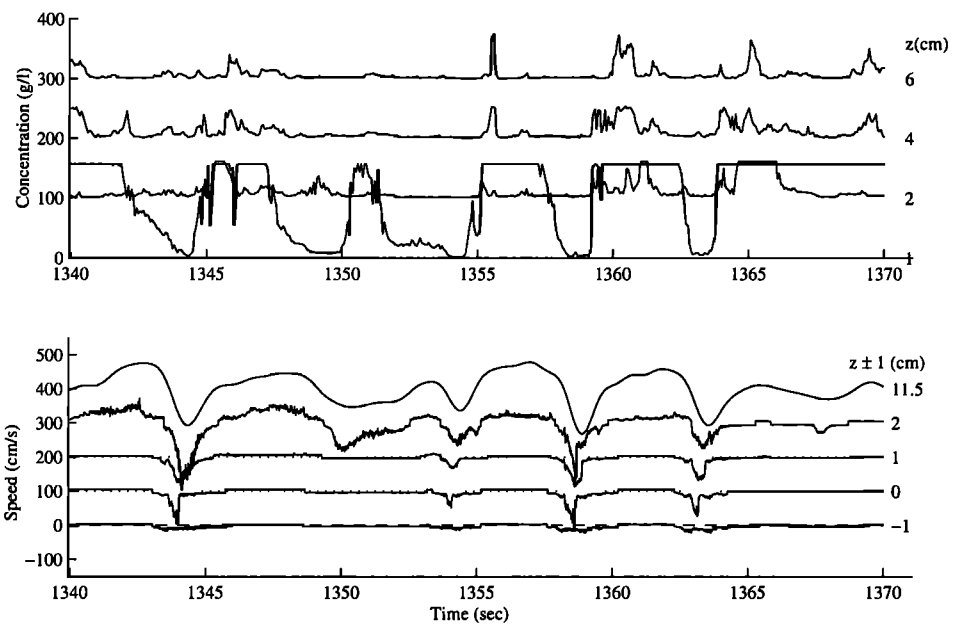

Figure 10. A 30 s time series of (top) velocity and (bottom) concentration showing a temporary bed mobilization or sensor insertion system vibration under several crests. Each velocity and concentration record is offset by 100 cm/s and 100 g/L, respectively. Notice that in each case a suspension event occurs following the erosion of the lowest FOBS sensor.

Table 2. Depth Root Mean Square Deviations between Two Models (u_{FGH} and u_S) and the Data (u_D) $z = z \pm \Delta z$ of the rms Velocity in the Five segments A–E

	A	B	C	D	E	Mean
$[\Delta u_{FGH_{rms}}(z-\Delta z)]_{rms}$	14.2	17.7	6.7	8.4	6	10.6
$[\Delta u_{FGH_{rms}}(z)]_{rms}$	6.9	11.8	9.7	10.6	14.1	10.6
$[\Delta u_{FGH_{rms}}(z+\Delta z)]_{rms}$	7.9	7.02	16.2	17.1	21.2	13.9
$[\Delta u_{S_{rms}}(z-\Delta z)]_{rms}$	14	19.1	7.4	8.9	5.9	11
$[\Delta u_{S_{rms}}(z)]_{rms}$	6.5	12.7	6.8	9.6	13.1	9.7
$[\Delta u_{S_{rms}}(z+\Delta z)]_{rms}$	8.3	6.5	13.6	16.3	20.5	13
$u_{\infty_{rms}}$	38.4	38.9	33.3	35.5	39.2	37.1

Here $z - \Delta z$ indicates the sensor array is Δz closer to the bed and $z + \Delta z$ indicates the sensor array is Δz away from the bed.

where α, β, and γ are known constants and $u_{rms}(z_o + \Delta z_1)$ and $u_{rms}(z_o + \Delta z_2)$ are the rms velocities at the two sensors closest to the bed. The constants are determined by performing Taylor series expansion (truncated to three terms) about z_o. Assuming the velocity at z_o is zero, the velocity gradient is approximated with

$$\left|\frac{\partial u}{\partial z}\right|_{z=z_o} \approx \sqrt{2}\left(-\frac{\Delta z_2}{\Delta z_1(\Delta z_1 - \Delta z_2)} u_{rms}(z_o + \Delta z_1) + \frac{\Delta z_1}{\Delta z_2(\Delta z_1 - \Delta z_2)} u_{rms}(z_o + \Delta z_2)\right). \quad (28)$$

Figure 11 shows the resulting shear velocity, u_{*log}, for each of the five data runs (A-E). The mean and standard deviation u_{*log} is 0.4±0.4 cm/s and corresponds to a mean friction factor ($f_w = 2u_*^2/u_o^2$) of 0.0001. The low value of f_w may be partially attributed to the slip condition on sand beds, which produces events of temporary bed mobilization, as seen in Figure 10.

The shear velocity was also estimated with the observations assuming a constant viscosity model in (23)

$$u_{*c} = \sqrt{\frac{\nu_c u_o (1+i)}{\delta_c}}, \quad (29)$$

for the sensor array located at the bed estimate ($u_{*c}[z]$) and also for the sensor array located at plus/minus the maximum possible deviation in the bed estimate ($u_{*c}[z \pm \Delta z]$) (Figure 11). The constant viscosity shear velocity mean and standard deviation for the three sensor array positions are 5.6 ± 2.1 cm/s ($z - \Delta z$), 9.3 ± 3.7 cm/s (z), and 13.5 ± 3.3 cm/s ($z + \Delta z$). There exists a significant variation of u_{*c} that depends on the true bed elevation. The friction factor, f_w, for the three array positions of the constant viscosity model are 0.04, 0.14, and 0.28, respectively, and are at least 2 orders of magnitude higher than the friction factor for (26).

A laboratory investigation of rough spilling waves on a fixed hydraulically rough bed yielded estimates of the friction factor inside and outside the breakpoint, with values that ranged from 0.02 to 0.04 [*Cox et al.*, 1996], at locations just inside and outside the breakpoint. The difference between these field observation and the laboratory observation estimates of the friction factor are significant considering the laboratory observations were made under conditions with an order of magnitude higher relative roughness (r/A).

Figure 11 (middle) shows the constant viscosity an estimate of the WBBL thickness, δ_c, from (23) for the three array positions. The means and standard deviations of the δ_c are 0.6 ± 0.4 cm ($z - \Delta z$), 1.7 ± 0.9 cm/s (z), and 3.5 ± 1.2 cm/s ($z + \Delta z$). The 95% confidence limits shows large scatter for the both estimates of the shear velocity and boundary layer thickness.

The representative shear velocity for the linear eddy viscosity model (5) and the linear time-varying eddy viscosity models are also shown in Figure 11. The representative shear velocity for the linear time-varying eddy viscosity FGH model was chosen as the amplitude $[\sqrt{(2)}u_{*FGH}(t)_{rms}$, where $u_{*FGH}(t)$ is defined in (16)], in a manner consistent with the *and Madsen*[1979] model which assumes the max-

Table 3. Depth Averaged Temporal Root Mean Square Deviations Between the FGH Model (u_{FGH}) and the Data (u_D) $z = z \pm \Delta z$ of the Time Varying Velocity in the Five Segments A–E

	A	B	C	D	E	Mean
$[\Delta u(z-\Delta z,t)]_{rms}$	15.9	18.5	8.9	8.7	8.8	12.2
$[\Delta u(z,t)]_{rms}$	13.1	15.2	12.2	10.8	14.7	13.2
$[\Delta u(z+\Delta z,t)]_{rms}$	14.2	18.0	21.7	17.9	23.3	19.0
$u_{\infty_{rms}}$	38.4	38.9	33.3	35.5	39.2	37.1

Here, $z - \Delta z$ indicates the sensor array is Δz closer to the bed and $z + \Delta z$ indicates the sensor array is Δz away from the bed.

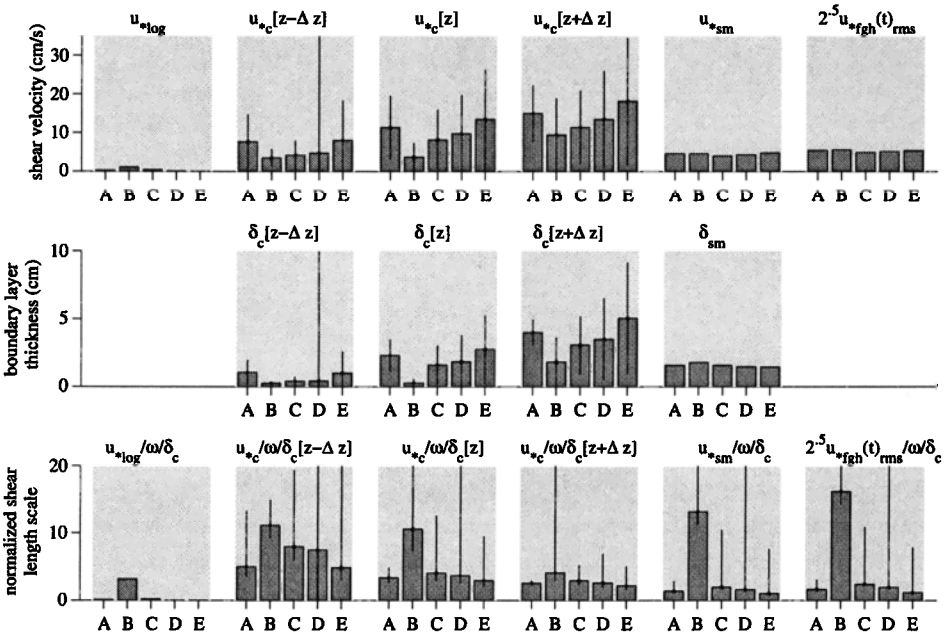

Figure 11. Ratio of the (top) shear velocity, (middle) boundary layer thickness, δ, and (bottom) normalized shear length scale $\frac{u_*}{\omega\delta}$ of the observations and models. Each panel of bars represents, from left to right: (1) log scaled boundary layer; (2) constant viscosity model with the sensor array shifted down by Δz; (3) constant viscosity model; (4) constant viscosity model with the sensor array shifted up by Δz; (5) linear eddy viscosity; and (6) linear time-varying eddy viscosity model. Error bars indicate the 95% confidence intervals for the fit of the observations to the constant viscosity model.

imum shear velocity is the appropriate mixing scale. The estimates of the bed shear velocity with the Smith model and FGH model vary only slightly over the five segments and are of comparable magnitudes, with means and standard deviations of $4.5 \pm .3$ cm/s and 5.4 ± 0.3 cm/s, respectively. The model predictions are significantly higher than $u_{*\log}$, are generally lower than u_{*c}, but are within the 95% confidence limits. Although the velocity shear at the bed is small ($u_{*\log}$) relative to the model estimates, these results indicate there is an increased mixing throughout the domain.

A further measure of the mixing is the shear length scale ($\sim u* /\omega$). In Figure 11, the six various estimates of the shear length scale are scaled by the constant viscosity boundary layer thickness, δ_c. From left to right, the mean values for each panel are 0.7, 7.3, 4.9, 2.9, 3.8, and 4.7. In most of the cases, the mean statistics are skewed by the low estimate of the boundary layer thickness in run B. The observational estimates of the shear length scale are at least a factor of 2 larger than the WBBL thickness scale. Also, the upper bounds of the 95% confidence interval would predict that this shear length scale may be as large as an order of magnitude higher than the boundary layer thickness. This suggests turbulence may be generated from sources other than bed shear.

4.3. Temporal Structure

The average vertical structure of the phase over each of the five segments was evaluated by determining the time of maximum correlation between each of the hot film velocities and the free stream velocity as measured by the EMCM (Figure 12). The cross correlation is restricted to a temporal resolution equal to the sampling interval of the EMCM (1/16 s). Furthermore, considering that the true response of the EMCM is 2 Hz, the 1/16 s interval is only valid for relative comparisons between the HF sensors. In agreement with simple WBBL theory, within the WBBL the velocity phase lead generally increases with decreasing sensor elevation. This relationship is readily apparent in Figures 5, 6, and 10. Time shifts of both boundary layer models also increase with proximity to the bed but are larger than the observations by approximately a factor of 2 (Figure 12). Both models predict a maximum velocity lead relative to that of the free stream velocity of 0.31 s at the bed ($\approx 25°$). The constant viscosity model predicts significantly larger phase shifts within the boundary layer than the other models and the observations.

The amplitude and phase structure of the velocity observations and the FGH model predictions are examined with frequency domain empirical orthogonal functions (CEOFs) of the cross-spectral matrix of segments A-E [*Wallace*, 1972] (Figure 13). The amplitude structure is qualitatively uniform over all frequencies, with a slight decrease in velocity shear with increasing frequency. If each frequency were acting independently, linear theory in (4) and (5) would predict that the boundary layer thickness would roughly be inversely proportional to the wave frequency. Of the four frequencies shown here, linear theory would predict that the boundary layer thickness should decrease from $11u*_o$ to $1.7u*_o$, indicating the frequencies are not independent of one another. The FGH model amplitude structure is in qualitative agree-

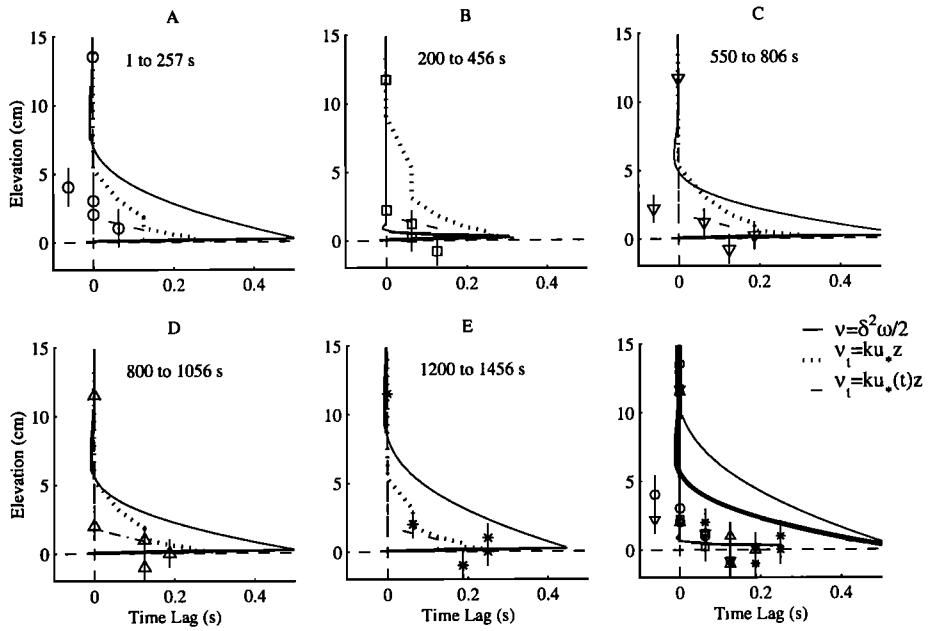

Figure 12. Time lag at maximum correlation between the EMCM and each HF over each segment (A-E) of the observations (various symbols), constant eddy viscosity model (solid curve), *Smith* [1977] linear eddy viscosity model (dash-dotted curve) and the FGH time-varying linear eddy viscosity model (dotted curve). Positive lags indicate a time lead. The vertical error bars indicate the maximum deviation of each quantity due to the maximum deviation in bed estimate about the observations. The bottom right-hand panel shows the lags of all of the observations and the constant viscosity model. Also, it shows the model results if the bed variation is moved plus/minus the maximum bed estimation error.

ment with observations and shows a decrease in the overall shear with frequency. As with the observations, the model does not show the decrease in boundary layer thickness that is predicted with linear theory.

The observations show that the phase shift, ϕ, at the incident peak ($\phi_o < 10°$) is significantly smaller than most model predictions of 25° and 45°. The incident peak phase shift is lower than the phase shift at both the subharmonics

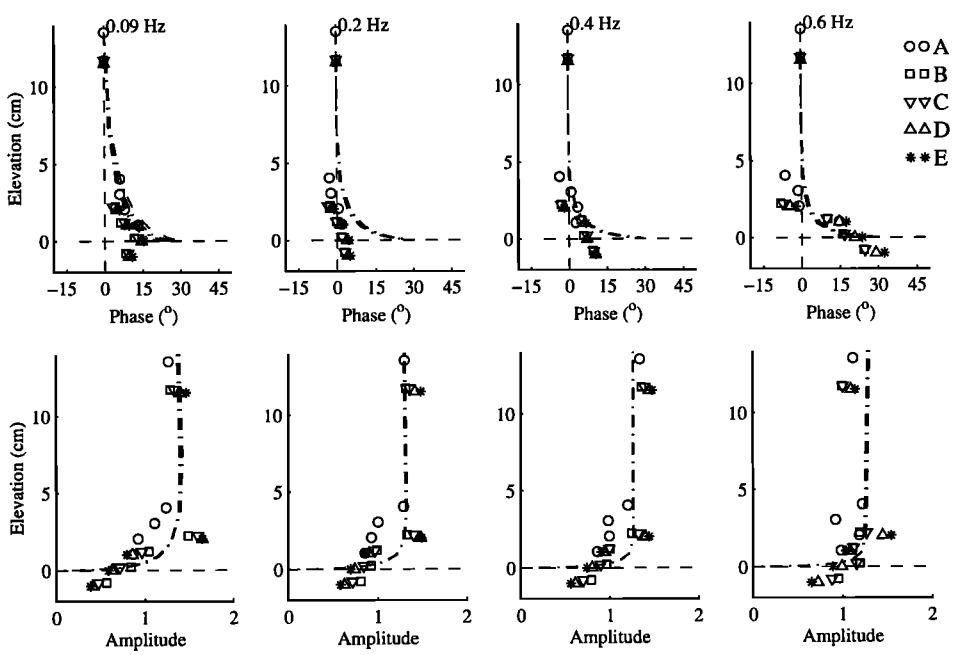

Figure 13. Complex domain empirical orthogonal function (CEOF) of the cross-spectral matrix at 0.09, 0.2, 0.4, and 0.6 Hz frequencies within the wave frequency band. At each frequency given in the upper panels is shown the (top) amplitude and (bottom) phasefor the (symbols) observations and (dash-dotted line) model. Each cross-spectral calculation is computed with 32 degrees of freedom. The incident peak occurs at 0.2 Hz.

and superharmonics and is in direct contrast to linear theory, which predicts that the phase shift at a particular elevation should decrease with increasing frequency as each sensor's relative position within the WBBL thickness increases. The observations show that at the highest frequency, ϕ_o is 30°. This also indicates that the frequencies are not acting independent of each other. Furthermore, the observations would suggest that the lead produced by the stress gradient is smaller than previously thought, and consequently, momentum is being mixed more rapidly within the boundary layer. This is also supported by the lower than expected shears present in the amplitude structure. This increase in the phase is characteristic of an increasing effect of the near-bed nonlinearities (FGH). The FGH model predicts a phase structure, which is relatively constant as a function of frequency. The FGH model shows qualitative agreement at 0.1 and 0.6 Hz but predicts significantly higher phase shifts at the dominant incident peak, 0.2 and 0.4 Hz. At an elevation of approximately 3 cm (the uppermost sensor in the HF array), there is a consistently larger velocity amplitude than the free stream and a small phase lead relative to the free stream. Although an increase amplitude may potentially be attributed to errors in calibration (see Figure 3), the phase lead cannot be attributed to such potential errors. This signal in amplitude and phase is consistent with a velocity overshoot.

5. Conclusions

In this paper, we presented a comprehensive set of observations that were used to investigate the amplitude and phase structure of the WBBL intermittently located within the surf zone and evaluate the theoretical scalings of boundary layer thickness and bed shear velocity. The observations were made on the Outer Banks of the North Carolina coast and collected during the collective Duck94 field experiment. Velocity observations were made with a vertical array of four hot film anemometers. Simultaneous bed level measurements were made with a fiber-optic backscatter sensor probe. Over a 34 min record, five 256 s time series were used to investigate the structure and dynamics of the wave bottom boundary layer.

The bed elevation was shown to vary over the course of the 34 min record. Even over shorter 4 min records, the critical bed stress was exceeded and the bed was temporally mobilized during extreme waves. This resulted in rms statistics that showed nonzero velocities at mean elevations, which were below the assumed bed elevation and smaller than predicted bed shears. This phenomenon made comparisons with simple models difficult, at best. Both statistical inferences of the observations and the models rely on an estimate of the bed roughness, z_o, which is difficult to measure under the simplest conditions and poorly constrained under movable beds.

The observational results of a decrease in rms velocity and an increase in phase with proximity to the bed are not inconsistent with oscillatory boundary layer theories. Some evidence exist for an overshoot region at an elevation roughly equivalent to the shear length scale. However, there exists several indications that suggest that momentum in the WBBL is being more rapidly mixed through the WBBL than simple theory predicted. First, as shown in the rms velocity and the frequency domain empirical orthogonal functions, smaller, near-linear vertical shears were present throughout the WBBL. This is also supported by the larger than predicted estimate of the shear velocity from the observations. Second, smaller phase shifts were found in both the averaged time leads and the frequency phase structure.

A nonlinear exchange of momentum was supported by the vertical structure of both the amplitude and phase as a function of frequency. If linear theory was valid, the observational results would show an increase in the sensor array's relative position within the boundary layer. Consequently, each sensor should show a decrease in phase and increase in amplitude relative to the free stream velocity. However, the phases were shown to increase with increasing frequency and the vertical shears were shown to decrease slightly, indicating the response of the WBBL is not independent of frequency.

Comparisons of the rms velocity and phase structure predicted by the two models showed essentially indistinguishable results. Depending on the true mean elevation of the bed, the rms deviation between the rms velocity observations and the FGH and *Smith* [1977] models ranged from 10.6 – 13.9 cm/s and 9.7 – 13 cm/s, respectively. Although the FGH model is computationally more intensive, it has the added appeal of predicting the WBBL temporal structure under a random wave field. The FGH model showed qualitative agreement with observations of the frequency structure of the velocity amplitude. However, predictions of the phase structure were not in agreement with the observations. Discrepancies between the model and the observations may be due to (1) the no-slip condition imposed at the bed, (2) neglecting the nonlinear advective terms, and/or (3) inadequate description of the actual mixing of momentum by the eddy viscosity closure. These observations are among the first coherent looks at wave bottom boundary layer in the nearshore region under conditions of significant sediment response and highlight the added complexity of the dynamics in natural environments.

References

Beach, R. A., and R. W. Sternberg, Suspended sediment transport in the surf zone: Response to incident wave and longshore current interaction, *Mar. Geol., 108*, 275-294, 1992.

Beach, R. A., R. W. Sternberg, and R. Johnson, A fiber-optic sensor for monitoring suspended sediment, *Mar. Geol., 103*, 513-520, 1992.

Conley, D. C., and D. L. Inman, Field observations of the fluid-granular boundary layer under near-breaking waves, *J. Geophys. Res.*, 97(C6), 9631-9643, 1992.

Cox, D. T., N. Kobayashi, and A. Okayasu, Bottom shear stress in the surf zone, *J. Geophys. Res.*, 101(C6), 14,337-14,349, 1996.

Davis, R.E., and L. Reiger, Methods for estimating directional wave spectra from multi-element arrays, *J. Mar. Res., 35*, 453-477, 1977.

Foster, D. L., Dynamics of the nearshore wave bottom boundary layer, PhD thesis, Oregon State Univ., Corvallis, 1996.

Foster, D. L., R. Guenther, and R. A. Holman, An Analytical solution to the wave bottom boundary layer equation, *Ocean Eng., 26*, 595-623, 1999.

Foster, D. L., R. A. Holman, and R. A. Beach, Correlation between sediment suspension events and shear instabilities in the bottom boundary layer of the surf zone, *in paper presented at Coastal Dynamics '94 Conference*, Am. Soc. of Civ. Eng., Barcelona, Spain, 1994.

George, R., R. E. Flick, and R.T. Guza, Observations of turbulence in the surf zone, *J. Geophys. Res.*, 99(C1), 801-810, 1994.

Grant, W. D., and O. S. Madsen, Combined wave and current interaction with a rough bottom, *J. Geophys. Res.*, 84(C4), 1797-1808, 1979.

Hino, M., M. Kashiwayanagi, A. Nakayama, and T. Hara, Experiments on the turbulent statistics and the structure of a reciprocating oscillatory flow, *J. Fluid Mech., 131*, 363-400, 1983.

Jensen, B. L., B. M. Sumer, and J. Fredsoe, Turbulent oscillatory boundary layers at high Reynolds numbers, *J. Fluid Mech., 206*, 265-298, 1989.

Jonsson, I. G., and N. A. Carlsen, Experimental and theoretical investigations in an oscillatory turbulent boundary layer, *J. Hydraul. Res., 14*, 45-60, 1976.

Justesen, P., Prediction of turbulent oscillatory flow over rough beds, *Coastal Eng., 12*, 257-284, 1988.

Madsen, O. S., Y. Poon, and H. C. Graber, Spectral wave attentuation by bottom friction: Theory. *paper presented at 21st Coastal Engineering Conference*, pp. 492-504, Am. Soc. of Civ. Eng., New York, 1994.

Nielsen, P., *Coastal bottom boundary layers and sediment transport*,324 pp., World Scientific, Singapore, 1972.

Sleath, J. F. A., Seabed boundary layers, in *Ocean Engineering Science*, edited by B.L.A.D.M. Hanes, pp. 693-728, John Wiley, New York, 1990.

Smith, J. D., Modeling of sediment transport on continental shelves, in *Marine Modelling*, edited by I. N. M. E. D. Goldberg, J. J. O'Brien, and J. H. Steele, pp. 539-577, John Wiley, New York, 1977.

Stokes, G. G., On the effects of internal friction of fluids on the motion of pendulums, *Trans. Cambridge Philos. Soc., 9, Part II*, 8-106, 1851.

Trowbridge, J., and O. S. Madsen, Turbulent wave boundary layers, 1, Model formulation and first-order solution, *J. Geophys. Res.*, 88(C5), 7989-7997, 1984.

Trowbridge, J. H., and Y. C. Agrawal, Glimpses of a wave boundary layer, *J. Geophys. Res.*, 100(C10), 20,729-20,743, 1995.

Wallace, J. M., Empirical orthogonal representation of time series in the frequency domain, II; Application to the study of tropical wave disturbances, *J. Appl. Meteorol., 11*(6), 893-900, 1972.

R. A. Beach, and R. A. Holman, College of Oceanic and Atmospheric Sciences, Oregon State University, Corvallis, OR 97331-5503.

D. L. Foster, Department of Civil and Environmental Engineering and Geodetic Science, Ohio State University, Columubs, OH, 43210-1275.

(Received October 8, 1996; revised October 12, 1998; accepted November 2, 1998.)